the substrate surface (*27*) with DOS of polymers could occur, or there could be charge transfer (*28*) based on the interaction between the polymers and the I-Au(111). These electronic interactions between the polymers and the surface might reduce the HOMO-LUMO gaps compared with those in solution.

References and Notes

1. A. K. Bakhshi, Deepika, *J. Mol. Struct.* **499**, 105 (2000).
2. T. Iyoda *et al.*, *J. Phys. Chem.* **95**, 5215 (1991).
3. H. Sirringhaus *et al.*, *Appl. Phys. Lett.* **77**, 406 (2000).
4. Y. Okawa, M. Aono, *Nature* **409**, 683 (2001).
5. S.-W. Hla, L. Bartels, G. Meyer, K.-H. Rieder, *Phys. Rev. Lett.* **85**, 2777 (2000).
6. R. Yamachika, M. Grobis, A. Wachowiak, M. F. Crommie, *Science* **304**, 281 (2004).
7. J. Barner, F. Mallwitz, L. Shu, A. D. Schlüter, J. P. Rabe, *Angew. Chem.* **115**, 1976 (2003).
8. M. Brun *et al.*, *Adv. Mater.* **16**, 2087 (2004).
9. M.-K. Ng, L. Yu, *Angew. Chem.* **114**, 3750 (2002).
10. M.-K. Ng, D.-C. Lee, L. Yu, *J. Am. Chem. Soc.* **124**, 11862 (2002).
11. H. Sakaguchi, H. Matsumura, H. Gong, *Nat. Mater.* **3**, 551 (2004).
12. Materials and methods are available as supporting material on *Science* Online.
13. G. Daoust, M. Leclerc, *Macromolecules* **24**, 455 (1991).
14. M. Leclerc, G. Daoust, *J. Chem. Soc. Chem. Commun.* **1990**, 273 (1990).
15. R. D. McCullough, *Adv. Mater.* **10**, 93 (1998).
16. T. Johansson, W. Mammo, M. Svensson, M. R. Anderson, O. Ingnäs, *J. Mater. Chem.* **13**, 1316 (2003).
17. G. Gigli *et al.*, *Appl. Phys. Lett.* **73**, 2414 (1998).
18. C. Roux, M. Leclerc, *Macromolecules* **25**, 2141 (1992).
19. M. Leclerc, *Adv. Mater.* **11**, 1491 (1999).
20. E. Mena-Osteritz *et al.*, *Angew. Chem. Int. Ed.* **39**, 2680 (2000).
21. B. Grévin, P. Rannou, R. Payerne, A. Pron, J. P. Travers, *Adv. Mater.* **15**, 881 (2003).
22. B. Grévin, P. Rannou, R. Payerne, A. Pron, J. P. Travers, *J. Chem. Phys.* **118**, 7097 (2003).
23. L. A. Bumm *et al.*, *Science* **271**, 1705 (1996).
24. L. A. Bumm, J. J. Arnold, T. D. Dunbar, D. L. Allara, P. S. Weiss, *J. Phys. Chem. B* **103**, 8122 (1999).
25. G. Barbarella, M. Zambianchi, A. Bongini, L. Antolini, *Adv. Mater.* **4**, 282 (1992).
26. A. Gesquière *et al.*, *Nano Lett.* **1**, 201 (2001).
27. M. Grobis, A. Wachowiak, R. Yamachika, M. F. Crommie, *Appl. Phys. Lett.* **86**, 204102 (2005).
28. M. Akai-Kasaya *et al.*, *Phys. Rev. Lett.* **91**, 255501 (2003).

29. This work was supported financially by the Ministry of Education, Culture, Sports, Science, and Technology (MEXT) Japan, the Japan Society for the Promotion of Science (JSPS), and the Asahi Glass Foundation.

Supporting Online Material

www.sciencemag.org/cgi/content/full/310/5750/1002/DC1
Materials and Methods
Figs. S1 to S4
References

26 July 2005; accepted 19 October 2005
10.1126/science.1117990

Structural Observation of the Primary Isomerization in Vision with Femtosecond-Stimulated Raman

Philipp Kukura, David W. McCamant,* Sangwoon Yoon, Daniel B. Wandschneider, Richard A. Mathies†

The primary event that initiates vision is the light-induced 11-cis to all-trans isomerization of retinal in the visual pigment rhodopsin. Despite decades of study with the traditional tools of chemical reaction dynamics, both the timing and nature of the atomic motions that lead to photoproduct production remain unknown. We used femtosecond-stimulated Raman spectroscopy to obtain time-resolved vibrational spectra of the molecular structures formed along the reaction coordinate. The spectral evolution of the vibrational features from 200 femtoseconds to 1 picosecond after photon absorption reveals the temporal sequencing of the geometric changes in the retinal backbone that activate this receptor.

Understanding the mechanism of a chemical reaction requires measuring the structure of the reactant as it evolves into product. Many of the most intriguing and efficient photochemical and photobiological reactions take place on ultrafast time scales and their kinetics have been well characterized by femtosecond absorption and fluorescence spectroscopies (*1*–*5*). Although x-ray diffraction is being developed for time-resolved structural studies of reactions, this approach is challenging to apply in the condensed phase and currently limited to processes slower than ~100 ps (*6*). Ultrafast vibrational spectroscopy is advantageous in this quest because it offers both excellent temporal and structural information (*7*). The traditional picosecond time-resolution limitation (*8*) is being transcended through the use of femtosecond pulses in the infrared (IR) in multidimensional as well as direct time-resolved experiments of ultrafast chemical and biological processes (*9*–*11*). The complementary Raman vibrational techniques have also advanced with the recent development of stimulated Raman in the femtosecond time domain (*12*, *13*), which is valuable because of its ability to interrogate biological processes in aqueous media. Here, we demonstrate the capabilities of femtosecond-stimulated Raman spectroscopy (FSRS) in studies of reaction dynamics by elucidating the molecular mechanism of the primary photochemical events in vision.

In FSRS, two laser pulses drive the Raman transition: a picosecond "Raman pulse" and a femtosecond broadband continuum "probe pulse" that stimulates the scattering of any vibrational modes with frequencies between 600 and 2000 cm^{-1}. The use of the additional probe pulse to induce the Raman scattering offers a number of notable improvements over traditional time-resolved spontaneous Raman spectroscopy (*14*), such as greatly enhanced cross sections and an order-of-magnitude improvement in time resolution (<100 fs) while maintaining excellent energy resolution (<15 cm^{-1}) (*15*, *16*). The impulsive creation of vibrational coherence by the Raman and probe pulses reveals highly time-resolved vibrational structural information that is not accessible by incoherent processes such as spontaneous Raman.

The primary step in vision is the photochemical cis-trans isomerization of the 11-cis retinal chromophore in rhodopsin (Fig. 1A). Production of the primary ground-state transient called photorhodopsin is one of the fastest photochemical reactions in nature and is complete in only 200 fs (*17*). As a consequence, the reaction is extremely efficient, with a quantum yield of 0.65, and about 60% of the incident photon energy is stored in the first thermodynamically stable all-trans retinal photoproduct called bathorhodopsin. This stored energy is then used to drive activating conformational changes in the G protein–coupled receptor that eventually lead to visual sensation. Although a number of theoretical models have been proposed (*18*–*20*) to explain rhodopsin's unique reactive properties, which are responsible for making it an excellent light receptor, many of the most critical questions about its photochemistry remain unanswered. For instance, the coordinates mediating fast excited-state decay, the role of the electronic excited state in the isomerization, the structure of retinal in photorhodopsin, and the nature of the reaction coordinate leading to bathorhodopsin are undefined.

We address these questions by acquiring femtosecond time-resolved vibrational spectra of retinal in rhodopsin throughout the reaction. Modeling of the vibrational structural features after rapid internal conversion to the ground state reveals the highly distorted structure of photorhodopsin. Surprisingly, a large fraction of the atomic rearrangement leading to the formation of fully isomerized bathorhodopsin is shown to occur in the ground electronic state. Vivid details of this

Department of Chemistry, University of California, Berkeley, CA 94720, USA.

*Present address: Department of Chemistry, Northwestern University, Evanston, IL 60208, USA.
†To whom correspondence should be addressed. E-mail: rich@zinc.cchem.berkeley.edu

structural evolution are revealed by the changing frequencies and lineshapes of key vibrational modes during the reaction.

FSRS spectra of rhodopsin after excitation with a 30-fs photochemical pump pulse centered at 500 nm are presented in Fig. 1B (*21*). The reference vibrational spectrum of rhodopsin (bottom) includes the symmetric C=C ethylenic stretch at 1548 cm^{-1}, the fingerprint region from 1100 to 1300 cm^{-1} due to structurally sensitive C–C single-bond stretching and C–H rocking modes, and a feature at 969 cm^{-1} due to concerted hydrogen-out-of-plane (HOOP) wagging motion of the 11 and 12 hydrogens (*22*). The bathorhodopsin reference spectrum at the top of Fig. 1B illustrates the isomerization-induced changes in the intensity and frequency pattern in the fingerprint region as well as the HOOP region; the original mode at 969 cm^{-1} is red shifted and split into three separate peaks at 920, 875, and 850 cm^{-1}, assigned to isolated C_{11}–H, C_{10}–H, and C_{12}–H wagging modes, respectively (*22*).

The fingerprint pattern of photorhodopsin at 200 fs appears to be midway between those of 11-cis rhodopsin and all-trans bathorhodopsin. The features evolve into the bathorhodopsin spectrum over the next 800 fs. In particular, the peak at 1267 cm^{-1} decreases in intensity, whereas the bands at 1216 and 1237 cm^{-1} remain virtually unchanged. Surprisingly, we observed very intense, dispersive lineshapes in the HOOP region between 800 and 950 cm^{-1} at early times. The dispersive HOOP features evolve on the same time scale as the fingerprint bands into the expected three positive features of the bathorhodopsin spectrum. By 1 ps, vibrational cooling has narrowed and blue shifted all features, including the ethylenic stretching band, thereby completing the transformation to bathorhodopsin. These data show that there is considerable reactive evolution on the ground-state surface from 200 fs to 1 ps.

The dispersive lineshapes in the HOOP region at early time delays originate from our capability to monitor structural evolution on the time scale of the reaction in a coherent fashion. This observation can be understood by considering how stimulated Raman signals are generated (*13*). The simultaneous action of picosecond Raman and femtosecond continuum probe pulses drives vibrational coherence in the sample (Fig. 2A). The gating of this process relative to the photochemical pump is temporally well defined by the short (~20-fs) probe pulse. The subsequent coherent vibration of the molecules modulates the macroscopic sample polarization in the time domain, thereby giving rise to positive definite Stokes and anti-Stokes features in the energy domain. Because we detected these features through interference with the unscattered probe, the signal appears on top of the probe envelope. However, if the frequency of this coherent motion initiated by Raman and probe pulses changes during the vibrational dephasing time as shown in Fig. 2B, where the oscillator is chirped from low to high frequency, then the resulting lineshapes become dispersive. The specific lineshape in Fig. 2B, with a negative feature on the high-energy side, is distinctive of a shift from a low- to a high-frequency vibration during the free-induction decay of the vibrational oscillator (*21*). Thus, the dispersive HOOP modes directly report on the dynamic structural relaxation of retinal as it evolves from the high-energy photorhodopsin transient to the ground-state bathorhodopsin product. The heterodyne detection scheme in FSRS is powerful in that it makes possible the observation of vibrational phase and frequency shifts that occur on a time scale shorter than the vibrational dephasing time.

We have simulated the spectral evolution of the HOOP features after internal conversion to the ground state using theory encompassing the above concepts (*21*). The frequencies of three

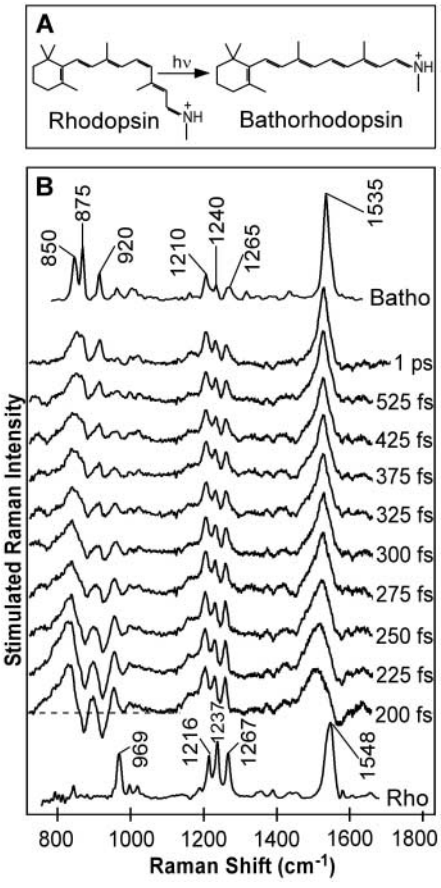

Fig. 1. (**A**) The primary event in vision: 11-cis retinal in rhodopsin is isomerized upon photon (hν) absorption to the all-trans bathorhodopsin photoproduct. (**B**) Time-resolved femtosecond-stimulated Raman spectra of rhodopsin from 200 fs to 1 ps. The spectra are vertically offset and ground state and solvent features as well as a broad sloping baseline have been subtracted (*21*). Resonance Raman spectra of ground-state rhodopsin (Rho) and the trapped bathorhodopsin (Batho) product are included for comparison. The dashed line in the 200-fs plot indicates the spectral baseline.

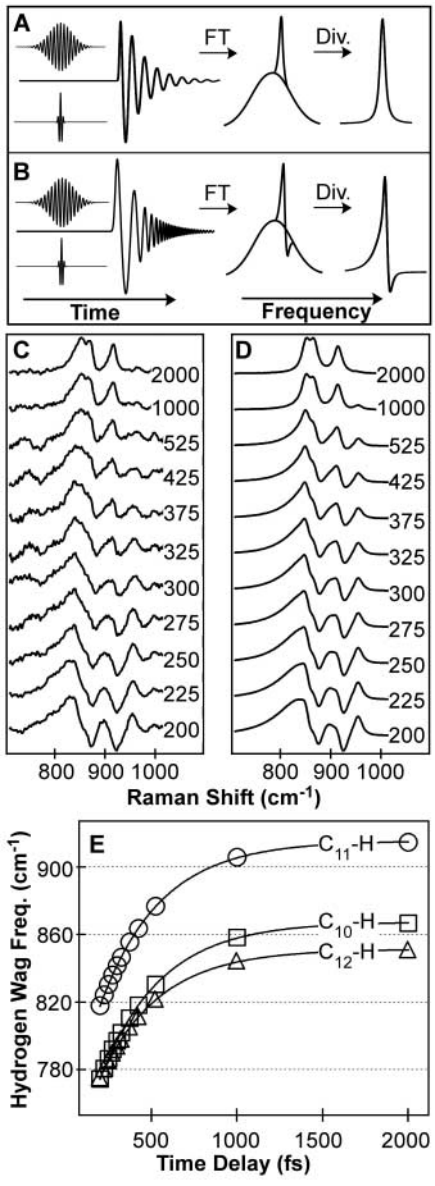

Fig. 2. (**A**) Picosecond Raman and femtosecond probe pulses drive vibrational coherence in the sample. Heterodyne detection yields a gain feature on top of the probe envelope in the energy domain shifted in energy relative to the Raman pulse according to the frequency of the vibration. Division (Div.) of spectra in the presence of the Raman pulse by spectra in its absence results in Lorentzian vibrational features. (**B**) An increase in the vibrational frequency during the vibrational dephasing time gives rise to dispersive lineshapes due to phase-sensitive heterodyne detection of the stimulated Raman signal. FT, Fourier transform. (**C**) Time-resolved stimulated Raman spectra of the HOOP region of reactive rhodopsin from 200 fs to 2 ps. (**D**) Simulated spectra of the HOOP region obtained from a four-mode model using three time-dependent frequencies, as in (**B**). (**E**) The simulations reveal a ~100 cm^{-1} blue shift of the C_{10}–H (□), C_{11}–H (○), and C_{12}–H (Δ) frequencies from 200 fs to 2 ps with a ~325-fs time constant.

modes resulting from isolated C_{10}–H, C_{11}–H, and C_{12}–H wagging motion were varied exponentially, and a fourth resulting from vibrationally excited but unreactive ground-state species was held constant at 959 cm^{-1}. This simple model is remarkably successful at reproducing the observed spectral dynamics in Fig. 2C. Not only do the simulated spectra duplicate the initially highly dispersive lineshapes, but they also reproduce the temporal evolution of these bands into the traditional bathorhodopsin features (Fig. 2D). The model also yields transient vibrational frequencies of structures along the pathway from photorhodopsin to bathorhodopsin. The HOOP frequencies increase by ~100 cm^{-1} from 200 fs to 2 ps with a ~325-fs time constant (Fig. 2E). Notably, all spectra were simulated with a single set of parameters that are not adjusted to fit the individual time points. The validity of our model is reinforced by the quantitative agreement between experiment and theory in light of the highly constrained parameters used in the simulations.

The evolution of the vibrational structure from 200 fs to 1 ps demonstrates that a large fraction of the net motion along the isomerization coordinate occurs on the ground-state surface. The most marked spectral change on this time scale occurs in the HOOP region where a ~100-cm^{-1} blue shift occurs with a ~325-fs time constant. We recently used vibrational modeling to demonstrate a close relationship between the degree of distortion of the polyene backbone and the anomalously low C_{12}–H wagging frequency in bathorhodopsin (*23*). Specifically, the frequencies of the C_{11}–H and C_{12}–H wagging modes in bathorhodopsin were explained by, at a minimum, the concurrence of same-sense 40° twists about the C_{11}=C_{12} and C_{12}–C_{13} bonds. This previous work suggests that the reduced HOOP frequencies in photorhodopsin are due to even greater distortions of the polyene backbone. The large HOOP frequency increases in the photo-to-batho transition are also physically reasonable because the restoring force for out-of-plane hydrogen wagging motion should increase as the double bonds strengthen in the more planar bathorhodopsin product state.

To test this explanation, we extended the approach of Yan *et al*. (*23*) by using density functional theory (*24*) to calculate the Raman frequencies for intermediate retinal structures that describe the photo-to-batho transition. Structures with calculated wagging frequencies that were in good agreement with the experimental results are presented in Fig. 3. The bathorhodopsin structure is twisted by –144° about the C_{11}=C_{12} and by 31° about the C_{12}–C_{13} bond, consistent with our earlier results, which only considered the position of the C_{12}–H wag. Fitting all the wag frequency reductions requires additional twists about adjacent bonds. Bathorhodopsin exhibits intense lines in the Raman spectrum at 850, 875, and 920 cm^{-1} assigned to isolated C_{12}–H, C_{10}–H, and C_{11}–H wagging modes, respectively. Vibrational calculations for the bathorhodopsin structure in Fig. 3C yielded features at 849, 857, and 881 cm^{-1} in excellent agreement with experimental data, except for an underestimated C_{11}–H wagging frequency. The photorhodopsin structure is more highly distorted, in particular about the C_9=C_{10} (45°), C_{10}–C_{11} (25°), and C_{11}=C_{12} (–110°) bonds. With these larger twists, the overall shape of retinal is much more like that of 11-cis rhodopsin than all-trans bathorhodopsin, despite having a formally isomerized (110°) C_{11}=C_{12} bond. Transient frequencies of the isolated C_{10}–H, C_{11}–H, and C_{12}–H wagging modes obtained from the analysis of the 200-fs FSRS spectrum appear at 772, 811, and 762 cm^{-1}, respectively. Calculated frequencies for these modes with the use of the proposed photorhodopsin structure (Fig. 3B) show good agreement with experimental data for the C_{10}–H and C_{11}–H modes (814 and 844 cm^{-1}, respectively), although the C_{12}–H frequency is overestimated (853 cm^{-1}). An alternative, but overall similar structure was found in which the C_{10}–H and C_{12}–H frequencies were calculated to drop by ~70 cm^{-1} (835 and 798 cm^{-1}, respectively) with an overestimated C_{11}–H frequency. In general, structures featuring only very specific combinations of backbone twists exhibited large frequency decreases compared with the bathorhodopsin structure.

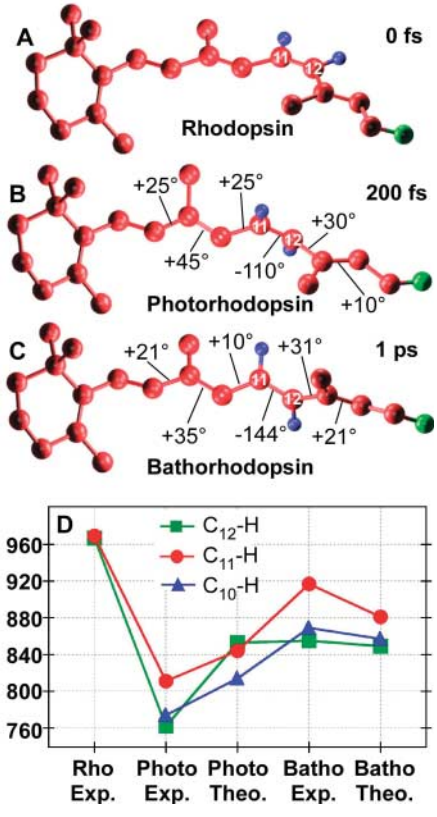

Fig. 3. (**A** to **C**) Retinal chromophore structures for reactant rhodopsin (*28*) and for photorhodopsin and bathorhodopsin that reproduce the observed hydrogen wagging frequencies. Backbone dihedral twist angles from the rhodopsin reactant are indicated. (**D**) Comparison of density functional theory (*24*) calculated (Theo.) and experimental (Exp.) hydrogen wagging frequencies for the photo and bathorhodopsin structures.

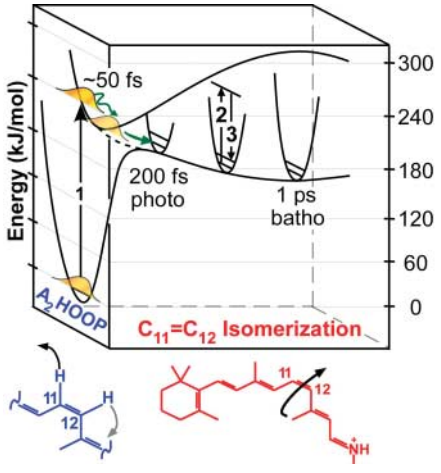

Fig. 4. Multidimensional representation of the isomerization coordinate for the primary event in vision. Absorption of a visible photon is followed by rapid motion out of the Franck-Condon region along high-frequency HOOP coordinates (vibrational period ~36 fs) which carry the system toward a conical intersection in ~50 fs. Curve crossing to the ground state to form highly distorted photorhodopsin is complete by ~200 fs. The structural evolution of retinal on the ground-state surface along the C_{11}=C_{12} torsional as well as other coordinates produces all-trans bathorhodopsin in ~1 ps. Also shown is the energy level diagram for coherent femtosecond-stimulated Raman probing of the ground-state molecular dynamics where (1) is a femtosecond photochemical pump pulse, (2) is a narrow bandwidth Raman pulse, and (3) is a broadband femtosecond probe.

Although future work certainly requires more detailed calculations that include protein interactions to provide more quantitative modeling of vibrational and energetic data, these results show that large-scale backbone distortions are capable of causing marked frequency drops in all the hydrogen wagging modes. The changes in vibrational structure observed by FSRS are thus best attributed to the dynamic ground-state relaxation of the initially highly twisted photorhodopsin structure as it evolves into bathorhodopsin.

Taken together, the data and modeling presented here are consistent with the following overall picture of the light-induced retinal isomerization that initiates vision (Fig. 4): The reaction begins with rapid excited-state decay after Franck-Condon excitation. Because optical excitation is strongly allowed, the transition from the A_g ground electronic state must populate an excited state having ungerade symmetry. Thus, any nuclear distortion that efficiently couples the Franck-Condon state to the ground state resulting in fast excited-state decay must be nontotally symmetric, such as the A_2 HOOP or backbone torsions. Critically, the isomerization can also only occur along nontotally symmetric coor-

dinates. The extremely short lifetime of the excited state (~50 fs), as established by transient absorption (*17*), resonance Raman intensity analysis (*25*), and spontaneous fluorescence measurements (*26*), however, severely restricts the extent of atomic displacements that can occur on this time scale. Given the energy available to the chromophore, the maximum C_{11}=C_{12} dihedral angle that can be achieved in 50 fs is ~50°, even if restrictions from the protein pocket are ignored (*25*, *27*). This suggests that the role of C_{11}=C_{12} torsional motion during the excited-state lifetime is limited. The similarity of the vibrational period of the 969 cm^{-1} $C_{11}H$=$C_{12}H$ HOOP (~36 fs) to the excited-state lifetime (~50 fs) supports its role in facilitating internal conversion. Additionally, resonance Raman intensity analysis shows quantitatively that retinal undergoes rapid distortion along the $C_{11}H$=$C_{12}H$ HOOP coordinate after optical excitation as a consequence of the lowered overall symmetry of the molecule when bound to rhodopsin (*25*). We thus conclude that excited-state decay through a conical intersection is mediated largely by fast HOOP motion.

Evolution along the C_{11}=C_{12} torsional coordinate after internal conversion leads to the formation of photorhodopsin with a formally isomerized (>90°) C_{11}=C_{12} bond but an overall highly distorted structure. Adjacent single- and double-bond twists compensate for the local cis-trans isomerization resulting in an overall reactant-like shape that, although isomerized about the C_{11}=C_{12} bond, minimizes steric interactions with the protein pocket, thereby enabling the fast reaction rate (compare Fig. 3, A and B). The molecule then uses the ~5000 cm^{-1} of energy available from rapid barrierless internal conversion as well as the ~3000 cm^{-1} from the photo-to-batho relaxation to drive the larger scale structural changes necessary to form the all-trans bathorhodopsin photoproduct in ~1 ps (Fig. 3C). Thus, although the isomerization is initiated in the excited state and photorhodopsin is formally trans about the C_{11}=C_{12} bond, much of the geometric changes associated with the isomerization actually occur on the ground potential surface in the photo-to-batho transition. This result is a direct consequence of the different time scales for complete excited-state decay (~200 fs) and bathorhodopsin formation (~1 ps) determined in this work.

This multidimensional model for rhodopsin isomerization, including a fast "gating" coordinate (HOOP), deviates substantially from the one-dimensional picture commonly used to describe photoisomerization reactions, where both electronic and nuclear dynamics occur along the same, slow torsional coordinate. Furthermore, these observations make it possible to better understand the role of the protein in determining rhodopsin's unique reactivity. The tight binding pocket influences the reaction path in three ways: (i) It primes the molecule for rapid excited-state decay along the HOOP coordinate by pretwisting the retinal backbone, (ii) it restricts the possible motion of the excited chromophore through steric interactions with surrounding amino acids, thereby promoting reaction speed and resulting in a high isomerization quantum yield, and (iii) it captures the high-energy bathorhodopsin product and efficiently transfers this energy into protein conformational changes that activate the receptor. We anticipate that these concepts will be important in understanding many efficient photobiological reactions.

References and Notes

1. C. V. Shank, *Science* **233**, 1276 (1986).
2. A. H. Zewail, *Femtochemistry* (World Scientific, Singapore, 1994).
3. G. R. Fleming, R. van Grondelle, *Curr. Opin. Struct. Biol.* **7**, 738 (1997).
4. M. M. Martin, J. T. Hynes, Eds., *Femtochemistry and Femtobiology: Ultrafast Events in Molecular Science* (Elsevier, Amsterdam, 2004).
5. L. Zhu, J. T. Sage, P. M. Champion, *Science* **266**, 629 (1994).
6. F. Schotte *et al.*, *Science* **300**, 1944 (2003).
7. M. D. Fayer, Ed., *Ultrafast Infrared and Raman Spectroscopy* (Marcel Dekker, New York, 2001).
8. H. Hamaguchi, T. L. Gustafson, *Annu. Rev. Phys. Chem.* **45**, 593 (1994).
9. M. C. Asplund, M. T. Zanni, R. M. Hochstrasser, *Proc. Natl. Acad. Sci. U.S.A.* **97**, 8219 (2000).
10. C. J. Fecko, J. D. Eaves, J. J. Loparo, A. Tokmakoff, P. L. Geissler, *Science* **301**, 1698 (2003).
11. S. E. Bromberg *et al.*, *Science* **278**, 260 (1997).
12. D. W. McCamant, P. Kukura, R. A. Mathies, *J. Phys. Chem. A* **107**, 8208 (2003).
13. S. Y. Lee, D. H. Zhang, D. W. McCamant, P. Kukura, R. A. Mathies, *J. Chem. Phys.* **121**, 3632 (2004).
14. Y. Mizutani, T. Kitagawa, *Science* **278**, 443 (1997).
15. The uncertainty principle is not violated because the broadband probe pulse in FSRS is dispersed and its multichannel detection is not time-resolved. In practice, the available information is only limited by the instrumental time resolution and our ability to model the experimental data.
16. W. T. Pollard, S. Y. Lee, R. A. Mathies, *J. Chem. Phys.* **92**, 4012 (1990).
17. R. W. Schoenlein, L. A. Peteanu, R. A. Mathies, C. V. Shank, *Science* **254**, 412 (1991).
18. A. Warshel, *Nature* **260**, 679 (1976).
19. R. S. H. Liu, *Acc. Chem. Res.* **34**, 555 (2001).
20. T. Andruniow, N. Ferre, M. Olivucci, *Proc. Natl. Acad. Sci. U.S.A.* **101**, 17908 (2004).
21. Materials and methods are available as supporting material on *Science* Online.
22. R. A. Mathies, J. Lugtenburg, in *Handbook of Biological Physics, Volume 3: Molecular Mechanisms in Visual Transduction*, D. G. Stavenga, W. J. DeGrip, E. N. Pugh Jr., Eds. (Elsevier, New York, 2000), pp. 55–90.
23. E. C. Y. Yan *et al.*, *Biochemistry* **43**, 10867 (2004).
24. M. J. Frisch *et al.*, Gaussian 03, Gaussian Inc., Pittsburgh, PA (2001).
25. G. R. Loppnow, R. A. Mathies, *Biophys. J.* **54**, 35 (1988).
26. G. G. Kochendoerfer, R. A. Mathies, *J. Phys. Chem.* **100**, 14526 (1996).
27. F. Blomgren, S. Larsson, *Chem. Phys. Lett.* **376**, 704 (2003).
28. K. Palczewski *et al.*, *Science* **289**, 739 (2000).

29. We thank S.-Y. Lee for many helpful discussions and S. Naghibzadeh for expert rhodopsin preparation. This work was supported in part by NIH grant EY-02051.

Supporting Online Material

www.sciencemag.org/cgi/content/full/310/5750/1006/DC1
Materials and Methods
Figs. S1 to S3
Table S1

3 August 2005; accepted 27 September 2005
10.1126/science.1118379

The Mid-Pleistocene Transition in the Tropical Pacific

Martín Medina-Elizalde[1,2] and David W. Lea[1,3]*

A sea surface temperature (SST) record based on planktonic foraminiferal magnesium/calcium ratios from a site in the western equatorial Pacific warm pool reveals that glacial-interglacial oscillations in SST shifted from a period of 41,000 to 100,000 years at the mid-Pleistocene transition, 950,000 years before the present. SST changes at both periodicities were synchronous with eastern Pacific cold-tongue SSTs but preceded changes in continental ice volume. The timing and nature of tropical Pacific SST changes over the mid-Pleistocene transition implicate a shift in the periodicity of radiative forcing by atmospheric carbon dioxide as the cause of the switch in climate periodicities at this time.

In the mid-Pleistocene, ~950 thousand years (ky) before the present (B.P.), the climate of Earth underwent profound changes in the length and intensity of its glacial cycles. This mid-Pleistocene transition (MPT), as indicated by benthic foraminiferal $\delta^{18}O$, was characterized by a change in the dominant periodicity of high-latitude climate oscillations from 41 ky to 100 ky; a positive shift in mean benthic $\delta^{18}O$, generally ascribed to continental ice-sheet expansion; and an increase in the amplitude variability of $\delta^{18}O$, attributed to more severe glaciations after 950 ky B.P. (*1*–*3*). Most of the hypotheses offered to explain these changes involve high-latitude Northern Hemisphere processes such as ice-sheet or sea-ice dynamics (*2*, *4*, *5*). Recent paleoclimatic reconstructions, however, have shown that during the MPT, the tropics also experienced major changes that resemble some aspects of high-latitude climate variability but also have their own unique patterns (*6*, *7*). Current hypotheses cannot fully explain these observations and the common

[1]Department of Earth Science, [2]Interdepartmental Program in Marine Science, [3]Marine Science Institute, University of California Santa Barbara, Santa Barbara, CA 93106–9630, USA.

*To whom correspondence should be addressed: E-mail: lea@geol.ucsb.edu